



Accelerated Wind-Turbine Wake Recovery Through Actuation of the Tip-Vortex Instability

Kenneth Brown,* Daniel Houck,† David Maniaci,‡ Carsten Westergaard,§ and Christopher Kelley¶
Sandia National Laboratories, Albuquerque, New Mexico 87123

<https://doi.org/10.2514/1.J060772>

Advances in wind-plant control have often focused on more effectively balancing power between neighboring turbines. Wake steering is one such method that provides control-based improvements in a quasi-static way, but this does little to fundamentally change the wake recovery process, and thus, it has limited potential. This study investigates use of another control paradigm known as dynamic wake control (DWC) to excite the mutual inductance instability between adjacent tip-vortex structures, thereby accelerating the breakdown of the structures. The current work carries this approach beyond the hypothetical by applying the excitation via turbine control vectors that already exist on all modern wind turbines: blade pitch and rotor speed control. The investigation leverages a free-vortex wake method (FVWM) that allows a thorough exploration of relevant frequencies and amplitudes of harmonic forcing for each control vector (as well as the phase difference between the vectors for a tandem configuration) while still capturing the essential tip-vortex dynamics. The FVWM output feeds into a Fourier stability analysis working to pinpoint candidate DWC strategies suggesting fastest wake recovery. Near-wake length reductions of >80% are demonstrated, although without considering inflow turbulence. Analysis is provided to interpret these predictions considering the presence of turbulence in a real atmospheric inflow.

Nomenclature

a	=	amplitude, deg or rpm
C_p	=	power coefficient
C_t	=	thrust coefficient
C_1, C_2	=	constants used in a semi-empirical model of near-wake length
c	=	local blade chord, m
D	=	rotor diameter, m
f	=	dynamic rotor rotational frequency, Hz
f_F	=	Fourier frequency, $j N^{-1}(\pi/\Delta\theta)f_0$, Hz
f_0	=	conventional rotor rotational frequency, Hz
h	=	axial separation of two adjacent tip helices, m
K	=	reduced frequency, $ac/2V_r$
k	=	nondimensional frequency of instability modes
N	=	number of flow snapshots
N_b	=	number of turbine blades
p	=	dynamic pitch control setting, deg
p_0	=	conventional pitch control setting, deg
R	=	rotor radius, m
r	=	local rotor radius, m
t	=	time, s
U_c	=	convection velocity of the tip vortices, m/s
U_∞	=	freestream velocity, m/s
u'	=	field of fluctuating (i.e., mean-subtracted) axial-velocity component, m/s

\hat{u}'_j	=	Fourier coefficients of u' , m/s
V_r	=	local relative velocity to the blade, m/s
x, y, z	=	Cartesian coordinates, m
α	=	angular frequency of actuation, rad/s
Γ	=	circulation of wake vortex filaments, m^2/s
θ	=	rotor azimuthal angle, rad
λ	=	tip speed ratio
σ	=	temporal growth rate of instability, Hz
σ^*	=	nondimensionalization of σ , $\sigma \times 2h^2\Gamma^{-1}$
ϕ	=	phase offset, rad
ω	=	wave number, $N_b(k - 0.5)$

Subscripts

a, b	=	axial locations in the flowfield
f	=	rotor-speed control
j	=	index of the integer-valued mode numbers from 0 to $N/2 - 1$
m	=	maximum
n	=	index of snapshots
nl	=	location of nonlinear threshold
p	=	pitch control

Symbols

$ \cdot $	=	magnitude of a complex quantity
$\ \cdot\ $	=	norm of a fluctuating quantity
$\bar{\cdot}$	=	revolution-averaged quantity

I. Introduction

A. Overview of Wind-Turbine Wake Recovery

ONE of the largest remaining opportunities to reduce the levelized cost of wind energy will come from substantial gains in the understanding of complex wind-plant aerodynamics and atmospheric phenomena, according to the U.S. Department of Energy [1]. As evidence, measurements over a range of modern wind plants across Europe [2] and in the U.S.A. [3] show that the second row of turbines in a wind plant captures around 20% less power than the first when the turbines are aligned with the wind, and this falls to around 40% for turbines located deep within the array. In stable atmospheric conditions, even higher losses have been observed [3]. Advances in wind-plant layouts and wake steering techniques have the potential to improve plant performance, but the turbine spacing is still fundamentally constrained by the recovery of the turbine wake. In addition

Presented as Paper 2021-1182 at the AIAA SciTech 2021 Forum, Virtual Event, January 11–15 and 19–21, 2021; received 9 April 2021; revision received 19 November 2021; accepted for publication 27 November 2021; published online 11 February 2022. Copyright © 2021 by the American Institute of Aeronautics and Astronautics, Inc. Under the copyright claimed herein, the U.S. Government has a royalty-free license to exercise all rights for Governmental purposes. All other rights are reserved by the copyright owner. All requests for copying and permission to reprint should be submitted to CCC at www.copyright.com; employ the eISSN 1533-385X to initiate your request. See also AIAA Rights and Permissions www.aiaa.org/randp.

*Senior Member, Wind Energy Technologies Department; kbrown1@sandia.gov.

†Postdoctoral Appointee, Wind Energy Technologies Department; drhouck@sandia.gov.

‡Principal Member, Wind Energy Technologies Department; dcmmania@sandia.gov.

§Senior Advisor, Wind Energy Technologies Department; chwest@sandia.gov.

¶Principal Member, Wind Energy Technologies Department; clkell@sandia.gov.

to this performance aspect, the turbulence of wakes significantly degrades the fatigue life of downstream turbines [4].

These problems can be traced back to the failure of the wake to fully “recover” from its depleted state after passing momentum to the turbine blades. During wake recovery, large-scale structures, such as those produced by instabilities over a mixing layer, entrain and inject a flux of mean-flow kinetic energy from the ambient flow into the depleted wake. Most of this reenergizing occurs in the far wake, which begins somewhere between 2 and 4 diameters downstream from the turbine [5,6] after a transition region following the near wake.

In the near wake, there exists a rich mix of relatively organized flow features that propagate downstream of a turbine. These coherent features include a region of velocity deficit on the scale of the rotor diameter, swirling motion opposite the rotation direction of the blades, an initially two-dimensional (2-D) wake structure from the tower shadow, helicoidally tracking vorticity (tip, root, and in-between), a columnar hub vortex, lateral spreading due to a pressure differential with the ambient flow, and entrainment of ambient flow promoting wake recovery, as well as any features that might be recognizable from the atmospheric boundary-layer (ABL) inflow. Ligarolo et al.’s [7] measurements showed that, within the near wake, the flow across the shear layer is governed by the periodic tip-vortex structures and results in a roughly zero net recovery of mean-flow kinetic energy, the helical tip vortices effectively shielding the wake from the ambient flow. Speeding the transition to the far wake via the breakdown of the tip vortices is thus critical for wake recovery, and this acceleration occurs through fluid dynamic instabilities in the wake as described next.

B. Some Inherent Wake Instabilities

The transition between near-wake and far-wake regions is triggered by instabilities in the wake and resulting breakdown of the tip vortices [8,9]. Theoretical analysis of tip-vortex stability offers the following three instability mechanisms: short-wave sinuous instability, long-wave sinuous instability, and mutual inductance instability [10]. The short-wave instability is due to the self-inductance of nearby locations on the vortex filament and results in localized “squiggles” along the filament. The long-wave instability is related to interactions between neighboring filaments that, when allowed to amplify, result in the mutual inductance (vortex pairing) instability [11] and the eventual “leapfrogging” of one vortex by another. It is this latter instability that has been shown to be the dominant cause of the beginning of wake breakdown downstream of wind turbines [7,9,12], propellers [8], and hovering rotors [13]. An excellent experimental flow visualization of the process was given by Alfredsson and Dahlberg [14], as shown in Fig. 1, along with a comparable lifting-line free-vortex method result from Marten et al. [15].

The hub vortex also plays a role in the tip-vortex evolution, as it has a stabilizing effect on the tip vortices. However, the hub vortex is

more short-lived than the tip vortex and therefore may not necessarily contribute to the tip-vortex mutual inductance breakdown [8,16]. (The results of [8], at least, suggest that the tip vortex destabilizes the hub vortex rather than vice versa.)

Several studies have demonstrated that the modes of the mutual inductance instability that result in maximum exponential growth correspond to half-integer multiples of the number of blades, that is, the disturbance of every other helical vortex is 180 deg out of phase [16–18]. The nondimensional wave number ω for each of these modes is the number of perturbation periods per rotor revolution as given by Eq. (1) [17]:

$$\omega = N_b(k - 0.5) \quad (1)$$

where N_b is the number of turbine blades and k are positive integers. (Note that some references, such as [11], use an alternate convention so that the quantity in the parenthesis is simply k .) The $k = 1$ (i.e., $\omega = 1.5$ for a typical three-bladed turbine, which corresponds to 1.5 perturbation periods per rotor revolution) mode has been found to be primarily responsible for the transition to the nonlinear instability growth regime that is characteristic of the beginning of the wake breakdown process [16]. This instability is evident mainly in the axial and radial directions, and the displacements in these directions are of the same order but 180 deg out of phase. Because of the phase difference, axial movements of a vortex filament toward its upstream neighbor coincide with the downstream movements of the neighbor, thus resulting in imminent pairing, after which the phase shift discontinues.

It is well documented that the location of the vortex pairing and breakdown is a function of the spacing between consecutive tip-vortex spirals that, in turn, is a function primarily of thrust coefficient and N_b [8,16,17], which are relatively well-converged design parameters in modern wind turbines. Also, recent experiments spanning a range of diameter Reynolds numbers from approximately 9×10^4 to 4×10^7 , and related both to wind energy [19,20] and propulsion [21], have validated that the streamwise distance before vortex breakdown (and therefore the beginning of the wake recovery) is inversely proportional to the magnitude of turbulent fluctuations, these fluctuations providing an initial perturbation to excite wake instabilities.

In the field, this inverse relationship is part of the driver for the correlation between the stability of the ABL and the length of wake recovery such that higher stability (i.e., less convective ABL conditions with consequently lower turbulence levels and less vertical mixing) produces slower recovery as has been shown both experimentally [22–25] and numerically [26–29]. Hancock et al. [22], for instance, measured the extent of the region with double-peaked velocity deficit to be $2.5D$ longer or 63% longer for a stable inflow than for an unstable one in a stratified-flow wind tunnel. The intentional wake forcing strategies to be described later in this paper are therefore most relevant for stable ABL conditions, which occur around 40–50% of the time as measured at sites both onshore [30] and offshore [31]. Offshore atmospheric conditions tend to have lower turbulence levels than onshore conditions across the stability regimes [26,32], which further stifles the wake recovery process for offshore wind plants.

Given knowledge of the dominant instability modes and their low initial magnitude in certain atmospheric conditions, a logical next step forward for wind-energy applications is to explore how these modes can be intentionally excited to promote wake breakdown and recovery.

C. Intentional Wake Mixing

While many wind-plant wake optimization studies focus on moderating the power extraction of “greedy” upwind turbines to yield a net plant-wide gain or on steering the wake of upstream turbines to avoid downstream ones, a different and ultimately more appealing strategy is to reduce the length of the wake recovery process. Because this recovery process siphons energy from the canopy above into the far wake below, speeding the onset of the far wake effectively increases the capture area of a wind plant with high power density.

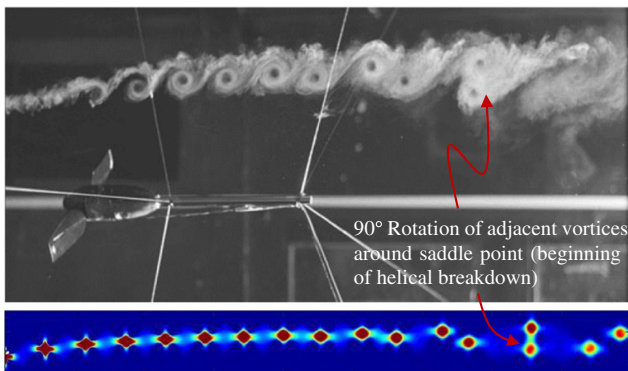


Fig. 1 Progression of a mutual inductance instability, or leapfrogging, event for tip vortices; smoke visualization from a two-bladed scaled model (top); reproduced from Alfredsson and Dahlberg [14]; snapshot of Q -criterion from a lifting-line free-vortex method (bottom); reproduced from Marten et al. [15]. (Reprinted by permission of AIAA)

One avenue to accomplish this goal involves unloading the blade tip by altering the blade induction distribution to speed the wake mixing process [33], although modification of the blade design does not allow any real-time control authority, besides via different combinations of collective pitch and rotor speed. In a similar vein, authors have investigated the effects of splitting the tip vortex with auxiliary surfaces near the blade tip, which could ultimately accelerate wake breakdown [34,35]. Another such static approach is the multirotor one, which splits the turbine area into several smaller rotors that may yield an overall faster wake recovery [36,37], but there is again no real-time control authority.

A more flexible approach has come into the spotlight in the last several years: dynamic forcing of the wake to excite instability modes. Much of the work related to this so-called dynamic wake control (DWC) approach has dealt with forcing frequencies that are appropriate for exciting bluff-body-type instabilities [38–43]. (No single terminology for this control approach has yet been unanimously accepted by the wind-energy community. Dynamic wake control may also be referred to as dynamic induction control, active wake mixing or active wake control.) Another DWC strategy, and one also with strong potential, is forcing of the mutual inductance instability described earlier using the triggering frequencies determined by Eq. (1).

Despite strong literature contributions on the physics of the growth of the mutual inductance instability, as reviewed earlier, relatively few studies have applied this knowledge and attempted to excite the instability. Several exceptions are described here. Following the numerical work of Ivanell et al. [16], Odemark and Fransson [44] demonstrated on a scaled wind turbine that the tip-vortex pairing processes are affected by periodic forcing from pulsed jets emanating from the hub into the wake. The vortex pairing process, which was observed to occur between 1 and $2.5D$ from the rotor, was associated with a shift in energy from the blade passing frequency to a lower frequency depending on the initial vortex strengths of the tip vortices trailing from each blade. Quaranta et al. [11], with a slightly more applied approach, modulated the rotor speed of a single-bladed scaled model and demonstrated that the leapfrogging position (swapping position in their notation) decreased by 60% as the initial tip axial displacement amplitude was increased from 1 to 15% of the distance between adjacent helices. Marten et al.'s [15] lifting-line free-vortex wake method (FVWM) also predicted a roughly 60% reduction in near-wake length by harmonic actuation of outboard flaps at an amplitude of 10 deg. The DWC strategies leveraged by Odemark and Fransson [44] and Quaranta et al. [11] were conducted in low turbulence environments with $\leq 1\%$ ambient turbulence intensity (TI ; given as a decimal not a percent), as DWC is likely to be most successful in lower turbulent environments, such as stable ABLs, where periodic forcing can compensate for the lack of natural unsteadiness to augment the initial instability magnitude. On the other hand, Marten et al.'s [15] results were made with 10% inflow TI , although their wake modeling ignored interaction between the original freestream vortices and the added wake ones.

Following in the path of the aforementioned work, the present study quantifies the benefit of DWC strategies that encourage wake recovery. The pioneering aspect of the work stems from the application of forcing using control vectors, blade pitch, and rotor speed control that are already available on all modern wind turbines to excite the mutual inductance instability. In contrast to a single previous study, where rotor speed control alone was studied in this capacity (i.e., [11]), the relatively inexpensive yet physically appropriate computational approach below permits a substantially more thorough exploration of the parametric space than was previously possible. For the other cases of blade pitch control and the tandem control approach to be described, no previous literature exists describing the excitation of the mutual inductance instability.

The formulation of the DWC forcing strategy is given in Sec. II. Section III describes the computational environment, which is enabled by multithreaded parallel computing combined with midfidelity modeling that captures the essential physics relevant to the tip-vortex instability. Section IV details results of parametric studies of forcing frequencies, amplitudes, and phases of the harmonic control actions.

For each flow simulation, a Fourier stability analysis offers insight on the instability growth rates and resulting near-wake lengths. Section V compares the effects of the DWC-induced instabilities with those of natural turbulent inflow, and concluding remarks are made in Sec. VI.

II. Dynamic Control Strategies

Our DWC strategy is to introduce an oscillation to the wake flow at an appropriate wave number to amplify the existing tip-vortex instability and accelerate wake breakdown and recovery. The following three control vectors exist on typical full-scale turbines: yaw, collective pitch, and rotor speed. State-of-the-art wake steering is based on quasi-static yaw offsets attempting to steer wakes away from downstream turbines. However, typical yaw rates of large turbines {maximum of 0.3 deg/s for the National Renewable Energy Laboratory (NREL) 5-MW [45]} are too slow to achieve any kind of meaningful oscillation amplitude that would be needed to gain active DWC authority at even the lowest integer k in Eq. (1). In addition, the mechanical wear on the yaw actuation system is unfavorable. On the other hand, both the blade pitch rates (maximum blade pitch rate of 8 deg/s for the NREL 5-MW [45]) and the generator speed control (maximum generator torque rate of 15,000 N · m/s for the NREL 5-MW [45]) provide ample authority for DWC strategies given a relatively steady inflow, where the dominant timescales of the flow, and thus the timescales of conventional control signals, are large with respect to the rotor period. Adjusting the rotor speed additionally gives the upside that the pitch system duty cycle, which is a common weakness of the turbine system, does not increase. However, torsional fatigue loads would increase on the drivetrain, which has yet to be evaluated.

For the DWC approach presented next, the dynamic pitch setting p (an increase in p corresponds to a reduction in blade angle of attack) relative to that of the conventional control setting p_0 is described by the following equation:

$$p = p_0 + a_p \sin(\omega_p \theta + \phi_p) \quad (2)$$

where a_p indicates the dynamic pitch amplitude, ω_p is the angular perturbation wave number described in Eq. (1), θ is the rotor azimuthal angle, and ϕ_p is any phase offset. The dynamic rotor rotational frequency f relative to that of the conventional control setting f_0 is described by the following equation:

$$f = f_0 + a_f \sin(\omega_f \theta + \phi_f) \quad (3)$$

where the subscript f is used to now distinguish between variables of the same names from Eq. (2).

It should be mentioned that rotor inertia is not considered and that blade pitch and rotor speed have no interaction with one another as implemented. The effects of rotor inertia, blade aeroelasticity, drivetrain dynamics, and pitch–speed interaction may factor into an eventual controller implementation and/or require co-optimization with DWC but are momentarily set aside to establish the fundamental control method feasibility.

III. Computational Setup

A. Reference Turbine

An example case of DWC will be demonstrated with the NREL 5-MW reference turbine [45]. The 126-m-diam turbine is operated at rated conditions with a uniform freestream velocity U_∞ of 11.4 m/s, f_0 of 0.202 Hz (12.1 rpm), tip speed ratio of 7, and p_0 of 0 deg. The airfoil data for the turbine come from the 2-D polars of [46], and no corrections are yet made for three-dimensional (3-D) effects. The arrangement of the eight airfoils into 17 spanwise segments as well as the variation in chord and twist along the blade span are given in [45]. In this study, we take the yaw angle, tilt angle, and precone of the turbine to be zero.

Differentiating Eq. (2) with respect to time and considering the maximum pitch rate of 8 deg/s for the NREL 5-MW [45], the maximum a_p attainable is 4.2 deg for the $k = 1$ case at the rated

rotation rate. Related to limits on the rate of rotor speed variation, the maximum generator torque rate is 15,000 N · m/s for the NREL 5-MW, as compared to the rated generator torque of 43,094 N · m [45].

With the introduction of dynamic actuation of blade pitch and rotor speed, the severity of unsteady blade aerodynamics on the NREL 5-MW should be gauged. The reduced frequency K is given by the following equation:

$$K = \frac{\alpha c}{2V_r} \quad (4)$$

where α is the angular frequency of the actuation [i.e., using the notation from Eqs. (2) and (3), respectively: $\alpha = \omega_p \dot{\theta}$ and $\alpha = \omega_j \dot{\theta}$], c is the local blade chord, and V_r is the local relative velocity to the blade. For $K \leq 0.05$, blade aerodynamics are classified to be quasi-steady, meaning that any unsteady effects are potentially negligible and at least very small [13,47]. Within the range $0.05 \leq K \leq 0.20$, notable lift hysteresis response can be expected, and beyond this, the lift hysteresis is dominant.

At the $k = 1$ value [lowercase k defined in Eq. (1)] that has been shown to be an optimal value for tip-vortex instability growth [15–18], $K \leq 0.05$ for the outer 30% of the NREL 5-MW at rated conditions. Furthermore, the notable hysteresis effects that are present between 25 and 70% should not have a first-order effect on the tip-vortex development given the relatively flat nature of the spanwise circulation distribution until 80% span for the NREL 5-MW case studied here (as will be shown in Sec. III.B.4). The dominant hysteresis threshold only occurs for the most inboard 6% of the profiled span, which is 19–25%. Based on these values, the formulations of the unsteady attached flow model and the unsteady separated flow (i.e., dynamic stall) model applied in our modeling to be described next are not taken to be principal concerns. (The truth of this statement for our turbine case can be further gauged from the comparison of cases with and without the dynamic stall model enabled in Fig. 6.)

B. Midfidelity Aerodynamic Model

1. First-Order Estimation Using FVWMs

Free-vortex wake methods are midfidelity aerodynamic simulations that are founded on the assumption that the regions of viscous-induced vorticity in the flow are concentrated to relatively small length scales. This allows the vorticity to be appropriately modeled as distributed singularities, and the viscous diffusion term can be dropped from the partial differential equation (PDE) of vorticity transport. By consideration of the vorticity transport PDE and Helmholtz's second law, the simple advection equation can be found that underlies the FVWM approach, which includes the time rate of change of the position vector of a Lagrangian marker (vortex segment) on the left-hand side and the sum of all the Biot/Savart-induced velocities and freestream velocity on the right-hand side [13]. Second-order accuracy of both sides of the advection equation can be achieved given an appropriate finite differencing scheme and a rotor angular discretization of less than 2.5–5 deg [48].

Vortex methods are well suited for the present analysis because the modeling simplifications leveraged to increase the computational efficiency of the methods do not have a first-order effect on the essential physics of the vortex pairing process, given that atmospheric effects are not modeled at this stage of the work. The simplified modeling of viscous effects, as noted earlier, is of relatively small consequence for the problem at hand because the mutual inductance instability is an inviscid phenomenon and one that has been well modeled previously by FVWMs applied to wind-turbine configurations at the same or lower Reynolds number as the one studied here [15,18]. The loss of accuracy after vortex pairing because of the absence of a turbulence model is also of small relevance to the present study that is concerned with only the initial vortex pairing process, although there is a need for follow-on work that includes turbulence modeling to account for atmospheric inflow turbulence as will be discussed. The restriction to uniform inflow profiles for many FVWM codes (including ours as discussed later), although no longer

necessary based on [49], is not a strong concern for our study either, which is primarily concerned with relative differences between cases, because the presence of a vertical shear profile does not affect the fundamental nature of the mutual inductance instability growth [50]. (Rather, it scales the growth rates based on local tip-vortex parameters, as described in the reference.) On the other hand, the primary benefit of the FVWM is its computational efficiency, which allows thorough exploration of parametric spaces that is not typically feasible on state-of-the-art actuator line large-eddy simulations that have computation times of four to five orders of magnitude greater than FVWMs [15].

As introduced earlier, the effectiveness of FVWM tools for analysis of tip-vortex stability was illustrated by several studies [15,17,18,51]. The first application was in the field of rotorcraft; see Bhagwat and Leishman [17]. These authors used the steady-state solution of an FVWM as the basis for a linear eigenvalue stability analysis that identified the $\omega = 0.5N_b$ instability mode as having highest amplification. For wind-energy applications, Rodriguez and Jaworski [18], Rodriguez et al. [51], and Marten et al. [15] also performed stability analyses on FVWM wakes but with time-marching rather than steady-state solutions being used to capture realistic transient wake geometries associated with floating offshore turbines, flexible blades, and flap actuation control, respectively.

Bhagwat and Leishman [17] also provided a cautionary note on using FVWM to study stability; numerically induced instabilities can be significant and can undo the second-order accuracy of an FVWM if not contained. For the time-marching methods that are required to model transient effects, the truncation error of higher-order terms in the explicit solution is an inevitable source of artificial instability. Other errors due to wake discretization, wake truncation, and viscous core models may be present in both time-marching and relaxation methods. These nonphysical instabilities should be, in general, minimized, as they may obfuscate the fluid dynamic instabilities of interest. Fortunately, given that the discretization of an FVWM is consistent with the governing equation of motion, convergence of the wake solution with increasing grid refinement is sufficient to demonstrate numerical stability. This requirement was met with an azimuthal step size of 5 deg for a time-marching algorithm in Bhagwat and Leishman [48].

It is inevitable that some numerical instability will remain. In a conventional FVWM without DWC, small numerical instability is in fact required to initially excite unstable modes from their state of (unstable) equilibrium [48], because FVWMs generally do not feature the inflow turbulence that is responsible for perturbing tip-vortex instabilities in the natural atmosphere. However, a difference in the character of the initial perturbation is likely to exist between the perturbations provided by the numerical instabilities and those of a real turbulent atmosphere. Thus, some FVWM predictions are less reliable in terms of the absolute locations of vortex pairing (which depend on the magnitude of the initial perturbation) [17], but the relative rates of disturbance growth predicted between different solutions in a parametric study are valid. In our study, much of this concern is minimized because the magnitudes of the DWC-induced perturbations are generally much larger than those of the numerical perturbations.

2. FVWM Baseline Implementation

In this work, we use the FVWM CACTUS developed for the study of wind and water turbines [52,53]. CACTUS is an adaption of the VDART3 code developed in the late 1970s [54] to model Darrieus-type vertical-axis wind turbines. A full overhaul, including modernizing the solution approach and extending the code to horizontal-axis geometries, was completed in the 2010s at Sandia National Laboratories [52].

The code uses a second-order predictor explicit time advancement scheme with a lifting-line solution for the blades and a lattice for the free wake. For the lifting line, circulatory unsteady aerodynamic effects for attached conditions are handled using the pitching flat-plate analogy [55]. Furthermore, two dynamic stall models are available in CACTUS, and we use the modified Boeing Vertol model [56] for all results unless otherwise noted. For the free wake,

uniform or linearly varying velocity profiles model the vortex cores, the former being employed in this work. Ground and tower effects can be modeled in CACTUS although are ignored presently. The current work is enabled using the OpenMP interface within CACTUS, and this capability may also benefit future studies involving larger numbers of simulations toward further detailed parameter sweeps of different DWC waveforms, frequencies, amplitudes, and duty cycles.

The case inputs for the CACTUS runs follow from the rated conditions of the NREL 5-MW, as well as the turbine and blade geometry, which were introduced in Sec. III.A. Note that the same spanwise discretization of the 17 aerodynamic stations for the NREL 5-MW has been used successfully in previous FVWM tip-vortex stability analyses [18,51,57] and will also be verified for our configuration in Sec. III.B.4.

The configuration inputs for the CACTUS runs are held at the default settings defined in [53] except for the following. The number of time steps between wake convection velocity updates is enforced to remain at the minimum of one. The number of azimuthal steps per rotor revolution was determined from the convergence study illustrated by Fig. 2. For all revolution counts studied, the revolution-averaged power coefficient \overline{C}_p (standard definition as described in [58]), converged to well within 10^{-3} by $2\pi/\Delta\theta = 80$ (azimuthal step size $\Delta\theta$ of 4.5 deg), where convergence at each revolution count is assessed relative to the \overline{C}_p of a reference simulation at $2\pi/\Delta\theta = 120$ ($\Delta\theta = 3$ deg) and the same revolution count. As 80 azimuthal steps per revolution not only achieves independence from the azimuthal resolution, as shown in Fig. 2, but also ensures second-order accuracy of the reconstructed velocity field [13], this step size was used for all subsequent simulations. Furthermore, the absolute \overline{C}_p was found to be sufficiently converged by 32 revolutions, which is thus taken as the precursor simulation length for all subsequent simulations. For all simulations, including the convergence study, wake points beyond 4 diameters downstream from the rotor plane were ignored for efficiency, a simplification that will produce less than 1% error in absolute \overline{C}_p according to analysis based on [59].

The data output from CACTUS occurred during revolutions 33–34 of the simulation, during which the velocity field was evaluated every two azimuthal steps on a 3-D grid of size 50 by 100 by 100 over the domain ranges of $0 \leq x/D \leq 5$, $-0.7 \leq y/D \leq 0.7$, and $-0.7 \leq z/D \leq 0.7$, respectively, where the coordinate system is defined in Fig. 3. The vortex filament positions and velocities were also saved during these final two revolutions.

The baseline case of the FVWM simulation without dynamic forcing is shown in Fig. 3. In accordance with the “horseshoe”-type vortex structure of vorticity typically observed on rotors, the trailing vorticity of the blades is primarily contained in the filaments at the extremes of the blade spans with opposite senses of rotation at each extreme. As introduced in Sec. I.B, we are primarily concerned with the tip-vortex filaments, and it is apparent that both of the two

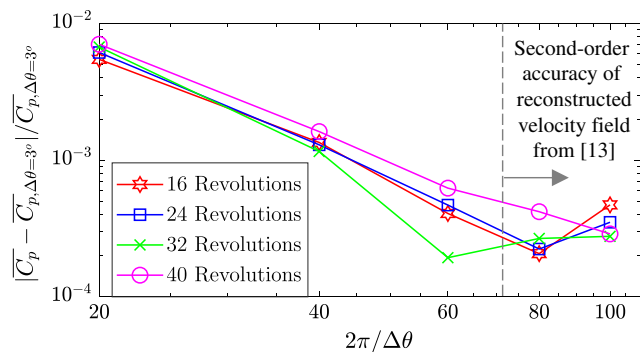


Fig. 2 Convergence study of revolution-averaged turbine power coefficient \overline{C}_p with increasing number of azimuthal steps per revolution, $2\pi/\Delta\theta$; different numbers of total revolution counts are indicated in the legend; each \overline{C}_p is referenced to the \overline{C}_p for the $2\pi/\Delta\theta = 120$ ($\Delta\theta = 3$ deg) case with the same respective number of total revolutions.

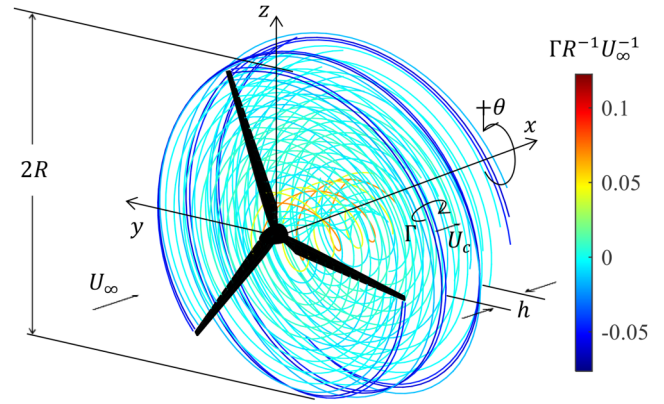


Fig. 3 Trailing vortex filaments from a baseline simulation with no dynamic forcing; the filament color indicates normalized circulation, Γ ; plotted data are restricted to one revolution for clarity; trailing filaments only are shown without the spanwise filaments; rotor geometry is for visual reference only and not representative of the NREL 5-MW used in the simulations.

outermost filaments emanating from each blade contain significant circulation. The separation of the trailing tip circulation into two distinct spanwise positions is due to the spanwise numerical discretization of the shed vorticity. Because the axial separation of two adjacent tip helices h (see Fig. 3) is around 10 times greater than the radial separation of the two outermost filaments in a helix sheet in our current modeling approach, any given axial pair of outer filaments may be considered to be in the far field of the circulation field of tip filament pairs on neighboring helix sheets. Consequently, the circulation from the outermost two filaments of a helix sheet will be lumped together when calculating the tip circulation to be used to normalize instability growth rates below.

3. FVWM Modifications

The code used in this work is a modified version of CACTUS that allows for dynamic actuation of blade pitch and rotor speed. The actuation is accomplished by updating the blade pitch and/or rotor speed at each azimuthal station according to Eqs. (2) and (3). The inputs for both actuation types thus include the frequency, amplitude, and phase offset of the control waveform. To verify the correctness of the coding modifications, traces of the quarter-chord angle of attack and local velocity at the blade from the modified CACTUS output, after removal of the induced velocity components, were found to match those implied by Eqs. (2) and (3). In the production runs, this unsteady forcing is applied for the full 34 revolutions of the simulation. Code modification has also been made to output velocity field data in the rotating frame of reference rather than the fixed frame of reference to aid the stability analysis to follow. For the cases with variable rpm, the rotating frame tracks the rpm of the turbine.

4. FVWM Verification and Validation

Given the initial application of VDART3 for vertical-axis wind turbines, the unsteady lifting-line formulation, including unsteady blade aerodynamics portions of this code (and its successor CACTUS), was well developed and validated from the beginning, including experimental comparisons of transient blade loading vs azimuth [54]. More recently, CACTUS has been employed for several horizontal-axis turbine studies, including code-to-code verification between the blade element momentum (BEM) code FAST and a servo-hydro-aerodynamic-coupled framework using the NREL 5-MW in CACTUS as performed for the OC3 test case [60]. This validation found strong agreement of unsteady aerodynamic quantities between the codes under pitch, heave, and surge platform motions for light rotor loading conditions, where a BEM approach as FAST is expected to be reliable [61,62]. In [63], a successful code-to-experiment validation of power, thrust, and torque performance from CACTUS with steady inflow

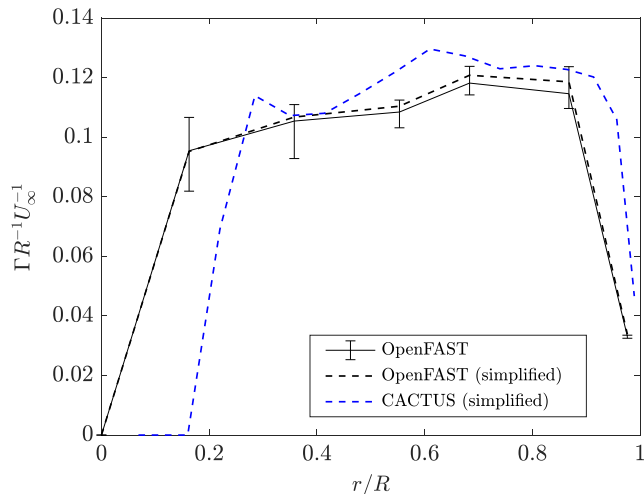


Fig. 4 Comparison of mean normalized blade circulation, Γ , vs normalized span position, r , from the OpenFAST BEM solution to the CACTUS FVWM solution for the NREL 5-MW at rated conditions; the error bars indicate the maximum and minimum values of the (unsimplified) OpenFAST solution.

is made vs water-tunnel measurements of a 1.22 m horizontal-axis rotor.

In this section, to demonstrate specifically the credibility of our implementation of CACTUS to accurately capture the spanwise blade loading distribution (and thus the shedding of vorticity into the wake) of the NREL 5-MW, we present further code-to-code verification of the steady CACTUS solution through a dedicated comparison with OpenFAST v2.4.0. The OpenFAST simulations are run for 10 min at 0.00625 s module time step with uniform, steady inflow and rpm at the rated conditions described in Sec. III.A. All AeroDyn and ElastoDyn inputs are the same as in the implementation found in [64] except for fields affected by updates to the input files to accommodate v2.4.0, and we also performed an alternate simulation with four simplifications to match our current unmodified CACTUS configuration, including removal of the tower effects, structural deformation, precone angle, and tilt angle.

Figure 4 compares the nodal blade circulations, which are averaged over the last 5 min of the simulation in the case of the full OpenFAST results to account for oscillations due to tower effects, structural deformation modes, and tilt, with the corresponding values from CACTUS. The normalized Γ values qualitatively match between the two codes, including the gentle increase in Γ from r/R of 0.3 to 0.7, followed by the region of nearly flat Γ from r/R of 0.7 to 0.9, and finally the drop toward zero at r/R of 1. The blade circulation distribution predicted by CACTUS is slightly more optimistic than that of OpenFAST, at least over the outer 70% of the blade span, but this does not discount the usefulness of CACTUS for studying tip-vortex dynamics, especially considering the agreement of the maximum normalized mutual inductance growth rates from CACTUS with the theoretical prediction as will be presented in figures throughout Sec. IV.

C. Fourier Stability Analysis

Previous work has found success using wake data from a variety of sources, including FVWMs as the basis for both linear eigenvalue stability analyses [17,18,51] and Fourier analyses [15,16,44,50] of tip-vortex divergence rates. We leverage both to demonstrate the effects of dynamic control actions on wake instability and near-wake length, although the Fourier analysis is used predominantly and is therefore the only one outlined in this section. Previous authors have implemented Fourier stability analyses by either extracting the maximum response of the frequency of interest (FOI) from the Fourier spectra at each cross section [16,50], or by integrating over the region of tip vorticity at the FOI [15] or over a band of frequencies centered

around the FOI [44]. Here, we follow closely the approach of Ivanell et al. [16].

Time-resolved cross-stream flow snapshots in the rotating frame of reference are temporally mean-subtracted to give the field of the fluctuating axial-velocity component \mathbf{u}'_n across each snapshot n . The \mathbf{u}'_n are transformed into the frequency domain to yield the Fourier coefficients $\hat{\mathbf{u}}'_j$ via Eq. (5):

$$\hat{\mathbf{u}}'_j = \frac{1}{N} \sum_{n=0}^{N-1} \mathbf{u}'_n e^{-2\pi i f_{F_j} (t_n - t_0)} \quad (5)$$

where N is the total number of snapshots, j is the index of the integer-valued mode numbers from 0 to $N/2 - 1$, f_{F_j} are Fourier frequencies given by the series $j N^{-1} (\pi / \Delta \theta) f_0$, and t is the time. [Because we have here taken the rotating frame to be one sampled based on a constant azimuthal rather than temporal increment, Eq. (5) is the nonuniform discrete Fourier transform.] The most unstable location within the annulus defined by $0.375 \leq r/D \leq 0.625$ where $r = \sqrt{y^2 + z^2}$ within each yz plane is $|\hat{\mathbf{u}}'_j|_m$, which is calculated according to Eq. (6):

$$|\hat{\mathbf{u}}'_j|_m = \max_{yz} |\hat{\mathbf{u}}'_j| \quad (6)$$

where the $|\cdot|$ notation denotes the magnitude of a complex quantity. For numerical reasons, the location of $|\hat{\mathbf{u}}'_j|_m$ at different axial locations may alternate between the three regions corresponding to the tip-vortex filaments trailing from each of the three blades. Note that the practice of taking the maximum of $|\hat{\mathbf{u}}'_j|$ at each j contrasts with the approach of Ivanell et al. [16], who took the y and z coordinates of $|\hat{\mathbf{u}}'_j|_m$ for the $k = 1$ case as the coordinates for the $|\hat{\mathbf{u}}'_j|_m$ of all the remaining k cases. Note that in some cases as follows, the index j will have a subscript of its own to denote a specific k frequency parameter of interest. For instance, $|\hat{\mathbf{u}}'_{j1}|_m$ refers to the $k = 1$ case.

The increase of $|\hat{\mathbf{u}}'_j|_m$ along the streamwise direction serves as an indicator of the growth of instabilities for each frequency component. Specifically, the ratio of $|\hat{\mathbf{u}}'_j|_m$ between two streamwise locations can be related to the temporal growth rate of an instability σ . The growth relationship takes the form of an exponential function in accordance with known character of the mutual inductance instability within its linear growth region [9,16]. (The linear region refers to that which shows linear growth using semilog plotting; see Fig. 5.) Equation (7) gives this relationship:

$$|\hat{\mathbf{u}}'_{j,b}|_m / |\hat{\mathbf{u}}'_{j,a}|_m = e^{\sigma(x_b - x_a) / U_c} \quad (7)$$

where U_c is the convection velocity of the tip vortices obtained by extracting the axial velocity of the vortex filaments within the linear region of growth from the FVWM results, and the subscripts a and b indicate two different axial locations in the flowfield. By performing linear regression on the linear growth region, σ is thus identified. The nondimensionalization of σ into σ^* is accomplished according to Eq. (8) [11]:

$$\sigma^* = \sigma \times 2 h^2 \Gamma^{-1} \quad (8)$$

where h is taken as a close approximation for the perpendicular distance between two consecutive filaments, and Γ is the circulation of the filaments. Strictly speaking, the oft-quoted maximum non-dimensional growth rate of $\sigma^* = \pi/2$ applies only to an infinite row of identical point vortices. For the more realistic case of a periodic array of inclined straight vortices, the value of σ^* for the NREL 5-MW at rated conditions is only 0.2% greater than the point vortex value for $k = 1$ according to the derivation of Quaranta et al. [11].

Before coming to the parametric studies and physical interpretations of the effects of control vectors in the following section, we here present the Fourier analysis as applied to an example wake with dynamic forcing to point out several key features of the Fourier analysis output. The control vector in this example case is rotor

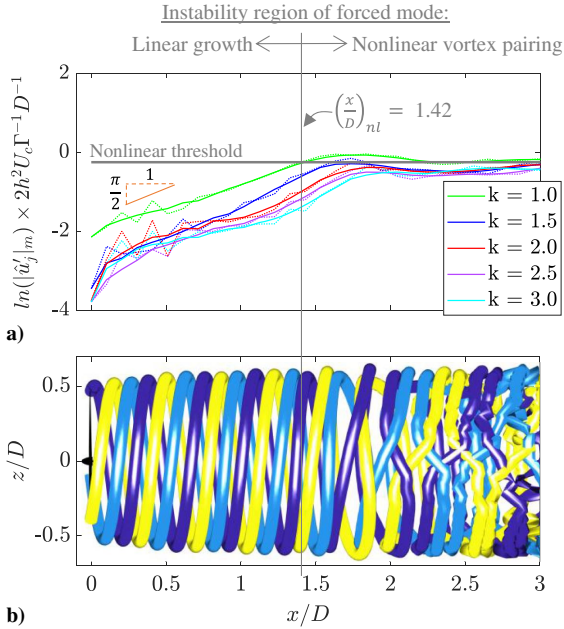


Fig. 5 Streamwise growth of instability for an example wake with DWC. **a)** Maximum wake instability Fourier coefficients, $|\hat{u}'_j|_m$, at each streamwise coordinate, x/D , for $a_f = 0.02$ rpm, $\omega_f = 1.5$ ($k = 1$), and $\phi_f = 0$; the dotted lines represent raw $|\hat{u}'_j|_m$, whereas solid lines are the moving average of the raw data taken with a window size of 5 points; normalization values are provided in the text; **b)** trajectories of the outermost tip-vortex filaments at an instant in time from the simulation in **a)**; the filament diameter does not possess specific meaning in this figure.

frequency, which is prescribed from Eq. (3) using $a_f = 0.02$ rpm, $\omega_f = 1.5$ ($k = 1$), and $\phi_f = 0$. Figure 5a describes the streamwise growth of the scaled and normalized tip-vortex instability magnitudes at five k values, including the forced frequency at $k = 1$. In the axis label as well as all following occurrences, division of $|\hat{u}'_j|_m$ by a reference value of 1 m/s is assumed to make the quantity inside the natural logarithm dimensionless. The $|\hat{u}'_j|_m$ are furthermore normalized before plotting to compare with the maximum nondimensional rate predicted by the classical $\pi/2$ vortex pairing result, as described earlier. Normalization values derive from the linear region of the baseline solution without any DWC, where $h = 14.1$ m, $U_c = 8.60$ m/s, and $\Gamma = 76.2$ m²/s, the former two being calculated as the mean between the two outermost filaments in a helix sheet and the latter as the sum over the two outermost filaments, as described previously. Smoothing of $|\hat{u}'_j|_m$ is applied with a moving average taken with a window size of 5 points, and this smoothing helps to account for variation in $|\hat{u}'_j|_m$ due in part to finite output grid resolution. Only the smoothed and not the raw results are shown in the remainder of the figures.

After an initial period of receptivity, the growth rate for the $k = 1$ forcing frequency remains close to the theoretically predicted $\sigma^* = \pi/2$ maximum until the nonlinear (nl) region is reached at $(x/D)_{nl} \approx 1.42$, wherein the flattening of the growth represents the onset of the tip-vortex pairing and breakdown event [16]. Finally, at around $x/D \approx 1.75$, the mutual inductance instability growth sees adjacent helices leapfrog one another. The leapfrogging event can be observed directly from view of the outermost vortex filaments themselves in Fig. 5b. Rather, sudden disorganization of the flow occurs within $1D$ of the vortex breakdown. Similarly to [16], we consider in this work the end of the near wake (i.e., the beginning of the transition region before the far wake) to be the location of a nonlinear threshold, where the linear growth ceases, which in our case is taken as $\ln(|\hat{u}'_j|_m) \times 2h^2 U_c \Gamma^{-1} D^{-1} = -0.25$.

The other k values besides the forced $k = 1$ case, which in the case of Fig. 5a are all harmonics of the forcing case, show fast initial growth before eventually attaining nearly the same growth rate,

although not the same magnitude, as the forced case. The nonforced k cases will not be plotted in the remainder of the paper.

IV. Stability Results

This section gives the Fourier analysis results on the sensitivity of the wake instability growth to the following three dynamic forcing parameters: frequency, amplitude, and phase. A subsection is devoted to each parameter.

A. Frequency Selection

This section aims to identify forcing frequencies of highest potential for wake length reductions. Although it may in fact be possible to force the wake with multiple superimposed waveforms of different frequencies and types to achieve optimal performance, we restrict the study in this paper to single-frequency harmonic cases, as described previously.

A frequency sweep was here performed using a similar example case as the one described in Sec. III.C employing dynamic rotor frequency with $a_f = 0.02$ rpm, $\omega_f = N_b(k-0.5)$, and $\phi_f = 0$ deg. The instability growth for different forcing k is plotted in Fig. 6a. The best-fit slopes of the linear region between $1.0 \leq x/D \leq 1.4$ are the σ^* for each k , and these are compared in Fig. 6b across all k .

Figure 6b depicts a clear trend in σ^* with peaks near integer k values and slow convergence of σ^* as k increases, both characteristics that are found for helices with small pitch in Widnall's [10] theoretical foundation on helical tip-vortex instabilities. Furthermore, σ^* distributions of similar character, including a maximum growth rate at $k = 1$, have been observed by previous authors studying rotor configurations using both Fourier analyses [15,16] and eigenvalue analyses [17,18,51]. The addition of the dynamic stall model tends to displace the σ^* curve to slightly higher k relative to the case without dynamic stall for k greater than roughly 1.5, although the location of maximum σ^* , $k = 1$, is unchanged with or without the model. In terms of absolute growth rates, this maximum σ^* is 1.41, or 10%, below the maximum theoretical value of $\pi/2$ for point vortices.

To further demonstrate the consistency of the Fourier result with other stability analysis techniques, an eigenvalue stability analysis for the unforced case on the outer filament of one blade was performed following Bhagwat and Leishman's [17] formulation. The same fluctuating and decaying trends are seen in the eigenvalue result as the Fourier one, including the maximum growth rate at $k = 1$. Some differences compared to the Fourier result may exist because each method resolves slightly different targets; the eigenvalue analysis is applied to filaments only in the tip region, whereas the Fourier analysis is calculated with velocities produced by the induction of all filaments in the flowfield. Because the eigenvalue analysis is performed on an unforced wake, the eigenvalue result matches most closely with the Fourier result that does not include dynamic stall.

Illustrations of all three outer filaments are provided in Fig. 6b for several k to aid in the causal analysis of the different growth rates. The graphics depict the effect of the various forcing frequencies on the outermost tip-vortex filament emanating from each blade at an instant in time in the FVWM results. As in Fig. 5b, the absolute filament diameter does not possess meaning and is scaled for visual clarity. However, in Fig. 6b and in other figures to follow, the relative variation in filament diameter is indeed meaningful and represents changes in the magnitude of the local circulation produced by the filament (see the following subsection for discussion on local circulation changes for DWC cases). For the illustrations of the three outer filaments in Fig. 6b, axial and radial displacements of these filaments relative to the unforced case are exaggerated by a factor of 200 for clarity, and corresponding differences in circulation as represented by filament diameter are exaggerated by a factor of 400.

For the $k = 1.5$ illustration, adjacent filaments are displaced in-phase so that the DWC-induced displacements are only a function of azimuthal location in the domain regardless of which filament is being considered. The result is a distortion of the whole helical structure, which makes each filament take on an s-shaped appearance, as shown. The dynamic forcing thus has little impact on the streamwise spacing between adjacent filaments, and the $k = 1.5$

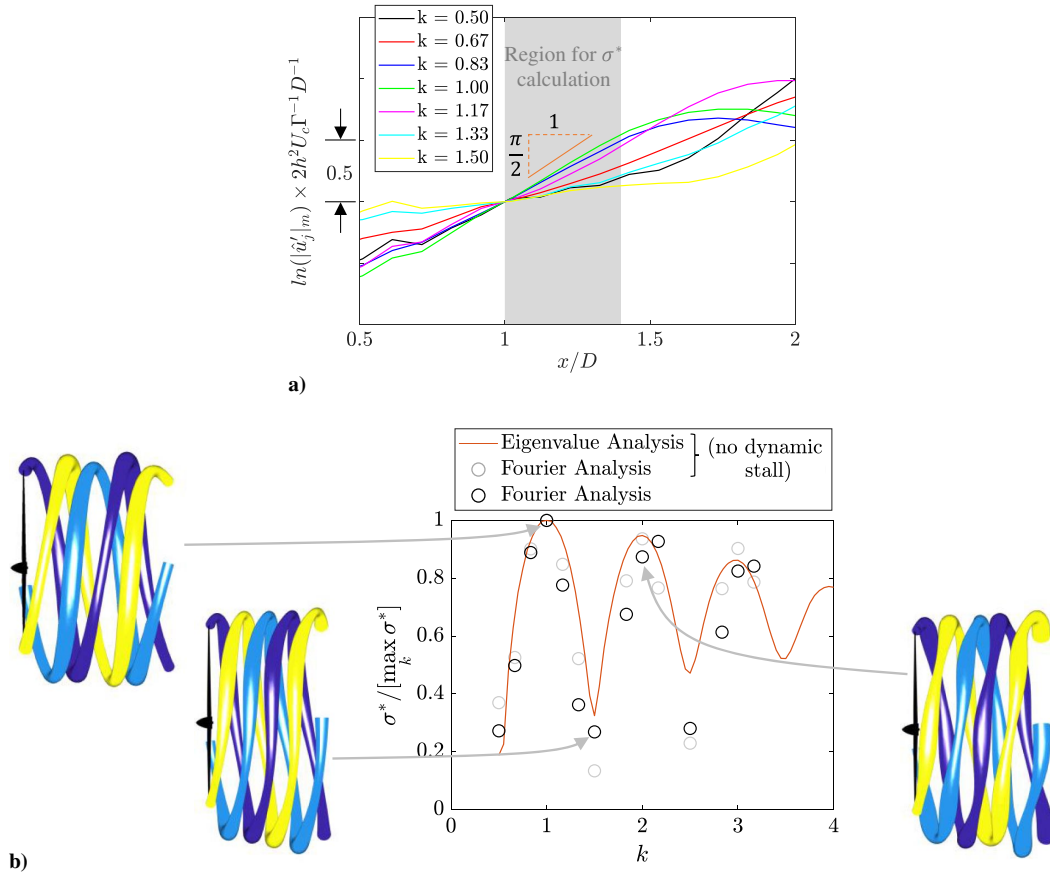


Fig. 6 Instability growth for different frequency parameters, k , as applied by varying rotor frequency with $a_f = 0.02$ rpm, $\omega_f = N_b(k - 0.5)$, and $\phi_f = 0$; a) the scaled, nondimensionalized, and smoothed maximum Fourier coefficients, $|\hat{u}'_j|_m$, vertically aligned at the streamwise location, x/D , of 1, whereas b) shows the scaled slopes calculated within the shaded region of a); comparison is made in b) between the Fourier growth rates and the corresponding rates calculated with the eigenvalue approach on tip-vortex filaments, see text for details of filament illustrations.

forcing therefore has a low growth rate. The same conclusions hold for larger half-integer k values.

On the other hand, integer-valued k forcing cases displace adjacent filaments to be out of phase by 180 deg of the perturbation cycle. Tracking a single vortex filament for the $k = 1$ case, it can be observed that a filament pairs with an adjacent filament every 120 deg of azimuth, and the pairing partner of the filament also alternates between every pairing position. For the $k = 2$ case, the pairing occurs every 80 deg of azimuth and again alternates between every pairing position. It could be said that the integer-valued forcing acts as a “matchmaker” between successive vortex filaments, prescribing the azimuthal location where two filaments will converge at instability hotspots. The $k = 1$ case will be used for all further results because of its highest magnitude growth rate.

B. Amplitude Study

Figure 7 contains individual studies of rotor speed and pitching amplitude in the first two rows, respectively, and a tandem amplitude study in the third row. In each case, the amplitude sweeps of a_f and a_p show a clear trend of decreasing near-wake length with increasing forcing amplitude. For the tandem case in Fig. 7c, we began by selecting pairs of a_p and a_f based on similarity of $(x/D)_{nl}$ from the nontandem results. For instance, the $a_p = 1.30$ deg case from Fig. 7b) is matched with the $a_f = 0.60$ rpm case from Fig. 7a, corresponding to $(x/D)_{nl}$ of 0.65 and 0.64, respectively. As will be justified in the following section, the relative phase shift of the two forcing waveforms is set so that $\phi_f = 90$ deg ahead of $\phi_p = 0$ deg. As will be discussed in Sec. V, many of the cases in Fig. 7 have the potential to shorten $(x/D)_{nl}$ relative to the turbulent near-wake lengths predicted by the model of Sørensen et al. [65].

The illustrations to the left of the plots depict the effect of the various DWC strategies on the tip-vortex filaments at an instant in

time in the FVWM results, and the same observations about filament behavior as made for the $a_f = 0.02$ rpm case with $k = 1$ in Sec. IV.A hold for the $a_f = 0.06$ rpm, $a_p = 0.13$ deg, and tandem cases illustrated in Fig. 7 (Note that in Fig. 7, axial and radial displacements of the filaments relative to the unforced case are exaggerated by a factor of 20 for clarity, and corresponding differences in circulation as represented by filament diameter are exaggerated by a factor of 40.). The primary visual difference between the three cases is the size of the DWC-induced filament displacements, which correlates with the respective instability magnitudes plotted on the right-hand side of the figure. The $(x/D)_{nl}$ variations between cases are thus related to the filament displacements at the instability hotspots, which see the paired filaments of the tandem case coming closer together than for the individual cases, a visual confirmation that the tandem case achieves the strongest filament-pairing effect for the amplitudes considered (although it likely produces significantly higher fatigue loading on the turbine, as well). In fact, the beginning of the mutual inductance leapfrogging event can already be seen in the large displacements of the blue and purple filaments at the downstream limit of the illustrated filaments in Fig. 7c. A difference in circulation magnitude is also apparent between pairing filaments at the instability hotspots, especially in Figs. 7b and 7c. Because the circulation magnitude between pairing filaments is 180 deg out of phase at any given azimuth, the mean circulation magnitude between any pair may be relatively constant.

It is relevant to note that the rate of instability growth within the linear region is the same to within a small percentage between all the cases in Fig. 7 because the growth rate for a specific frequency of forcing is an inherent characteristic of the rotor wake [48]. Rather, it is the differences in the initial amplitude of the instability for each case that cause the nonlinear regime to be reached at different x/D . For the cases involving dynamic pitch, the initial growth rate takes some

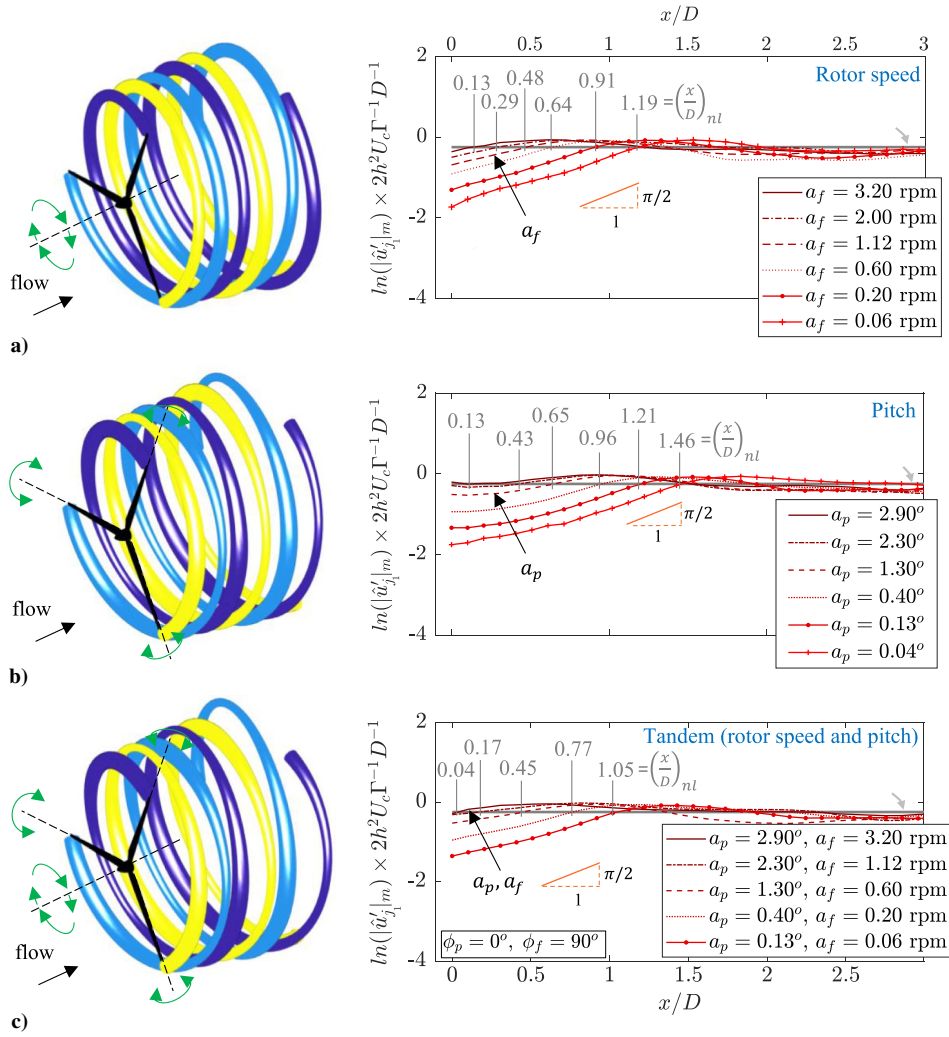


Fig. 7 a–c) Results of the $a_f = 0.06$ rpm, $a_p = 0.13$ deg, and $a_f = 0.06$ rpm/ $a_p = 0.13$ deg cases, respectively (left) Trajectory of the outermost tip-vortex filaments taken for the first two revolutions downstream of the rotor at an instant in time from the FVWM results (see text for details); (right) demonstration of control authority over the initial maximum wake instability Fourier coefficients, $|\hat{u}'_{j1}|_m$, as well as the growth along the streamwise coordinate, x/D ; all cases use $\omega = 1.5$ ($k = 1$), and the harmonic amplitudes a and phase angles ϕ are zero unless noted otherwise.

stretch of distance to adopt a mutual inductance-type linear growth, although the dynamic forcing clearly still increases the initial instability magnitude, thereby shortening the near-wake length.

C. Phase Study

Figure 8 gives the results from the tandem configuration of a sweep of ϕ_f with constant ϕ_p . Varying the relative phase between the rotor

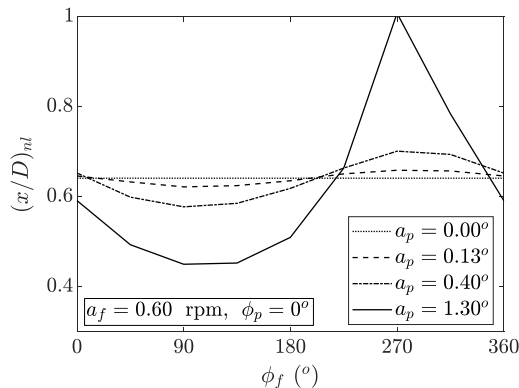


Fig. 8 Effect of rotor speed forcing phase ϕ_f on near-wake length $(x/D)_{nl}$ for a constant pitch forcing phase angle ϕ_p ; all cases use $\omega = 1.5$ ($k = 1$).

speed and pitch forcing indicates a preferential phase shift of ϕ_f between 90 and 135 deg ahead of ϕ_p that produces the most constructive superposition of forcing waveforms and resulting reduction of $(x/D)_{nl}$. This trend is constant across the range of a_p amplitudes studied in Fig. 8, although greater values of a_p for the given a_f clearly offer the greatest potential reduction of $(x/D)_{nl}$. For the largest a_p of 1.30 deg, the tandem result has a 30–31% lower $(x/D)_{nl}$ than either of the individual cases of the same forcing amplitudes.

V. Analysis/Discussion

The preceding FVWM modeling does not consider the effects of atmospheric turbulence in the rotor inflow on instability growth. Inflow turbulence introduces perturbations to the tip-vortex structures that may have an effect on wake instabilities that is comparable to the DWC actions studied earlier, depending on the TI . The question becomes, “How high can the TI be for the DWC actions to still be effective?”

The semi-empirical model of Sarmast et al. [9] incorporates a relationship between $(x/D)_{nl}$ and the inflow TI , as in Eq. (9):

$$(x/D)_{nl} = 8 \left[1 + C_2 \left(\sqrt{1 - C_t} - 1 \right) \right]^3 [N_b \lambda C_t]^{-1} \ln(C_1 TI) \quad (9)$$

where C_1 and C_2 are constants for which Sørensen et al. [65] found 0.33 and 0.52, respectively; C_t is the thrust coefficient (taken as 0.756

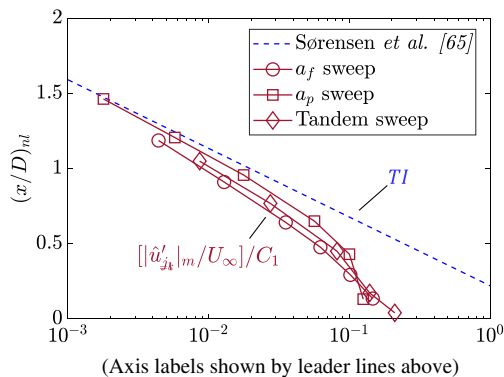


Fig. 9 Near-wake length, $(x/D)_{nl}$, vs turbulence intensity, TI , from Sørensen et al.'s [65] model (blue data) and scaled maximum axial perturbation magnitude, $[\hat{u}'_{j1}|_m/U_\infty]/C_1$, as calculated $0.1 D$ downstream of the rotor with DWC actions (red data).

from the FVWM results without DWC), N_b is the number of blades, and λ is the tip speed ratio. The equation is plotted in Fig. 9, for reference.

The C_1 constant is furthermore useful, as it is the constant of proportionality between a norm of the fluctuating axial-velocity field, $\|\hat{u}\|/U_\infty$, just behind the rotor blades and the corresponding TI . In light of the derivation of Eq. (9) that stems from the rotating sinusoidal axial tip forcing results of [16], one interpretation of $\|\hat{u}\|/U_\infty$ is as the maximum axial-velocity Fourier coefficient magnitude computed in the rotating frame of reference just behind a blade tip. If it is assumed that the maximum Fourier coefficient in the calibration data used for C_1 was the maximum growth rate case of $k = 1$, then we may set $\|\hat{u}\|/U_\infty$ equal to the value of $|\hat{u}'_{j1}|_m/U_\infty$ just behind the blades, which is conveniently already tabulated as a result of the preceding Fourier analysis. The proportionality relationship given in Sarmast et al. [9] and Sørensen et al. [65] could then be transcribed as $|\hat{u}'_{j1}|_m/U_\infty = C_1 TI$. This relationship allows the addition of the DWC data from Sec. IV.B to Fig. 9, where the value $[\hat{u}'_{j1}|_m/U_\infty]/C_1$ on the horizontal axis may be considered the effective (or artificial) turbulence level associated with the DWC actions. The $\hat{u}'_{j1}|_m$ is taken at the location $0.1 D$ downstream from the rotor plane. Note that uncertainty in the value of C_1 due to the assumption of $\|\hat{u}\|/U_\infty$ as the maximum Fourier coefficient manifests as uncertainty in the horizontal translation of the DWC data relative to the Sørensen et al. [65] line, although the slope of the data is not in doubt. The deviations of the DWC data from the semilog linear slope of the Sørensen et al. [65] model near the higher $[\hat{u}'_{j1}|_m/U_\infty]/C_1$ may indicate that there are effects present in the DWC flowfields that are not well described by the simple scaling between $|\hat{u}'_{j1}|_m$ and TI proposed earlier. These deviations also suggest that within the assumptions of the current analysis, the artificial turbulence added by DWC is relatively “more efficient” for a given perturbation magnitude than natural turbulence as the higher perturbation magnitudes are approached.

The general position of the tandem sweep curve between the individual sweep curves suggests that the tandem approach is not inherently superior to simply using an individual control vector in isolation, although structural quantities should also be investigated between the control vector approaches since $|\hat{u}'_{j1}|_m$ is at best a surrogate for some fluctuating thrust metric. Comparing the α_f sweep to the α_p sweep, the α_p sweep is less efficient than the α_f sweep in terms of the achieved $(x/D)_{nl}$ for a given input $|\hat{u}'_{j1}|_m$ over most of the range of $|\hat{u}'_{j1}|_m/U_\infty$ considered, that is, there is a vertical offset between the α_p and α_f curves for most of the plotted range. This behavior may be understood in light of the slow initial growth of the pitch-induced instability discussed for Fig. 7. However, the larger initial axial fluctuation magnitude of the dynamic pitch control approach could make this strategy more robust against the aperiodic interference of inflow turbulence, although much is still to be learned about the flow physics of the different DWC approaches. Initial

analysis on the effectiveness of DWC in the presence of inflow turbulence is given next.

From Fig. 9, it is clear that some DWC actions of smaller magnitude will not reach their predicted $(x/D)_{nl}$ before high inflow turbulence environments would cause the wake to already begin to breakdown. For instance, $(x/D)_{nl} = 0.8$ according to Eq. (9) for $TI = 0.10$, and so the DWC actions of the lowest six $[\hat{u}'_{j1}|_m/U_\infty]/C_1$ points plotted may have little effect on the $(x/D)_{nl}$ in such a case.

Figure 10 helps to visualize the potential benefit that different DWC magnitudes might have on $(x/D)_{nl}$ by cross-referencing with the $(x/D)_{nl}$ from the turbulent near-wake length model of Sørensen et al. [65]. The benefits in terms of relative $(x/D)_{nl}$ reductions are plotted vs the ratio of the perturbation magnitudes from the DWC to those from the inflow turbulence, $[\hat{u}'_{j1}|_m/U_\infty]/[C_1 TI]$. [Note that these plotted results are sensitive to the tuning of both the C_1 and C_2 constants in the model of Eq. (9).] As this ratio increases, the likelihood increases that the DWC-applied waveform will be initially coherent and will remain coherent downstream, and thus, the likelihood of the DWC actions to achieve the potential $(x/D)_{nl}$ reductions suggested by the nonturbulent FVWM results also increases. Note that the various colors are generated by changing TI , but this does not result in a pure horizontal shift because the reference value used in the calculation of the ordinate depends also on the TI (i.e., percent reduction in $(x/D)_{nl}$ is calculated relative to the $(x/D)_{nl}$ values of Eq. (9) for the given level of TI). However, for all inflow TI values, $(x/D)_{nl}$ reductions of over 80% are suggested for the maximum considered amplitude cases of $a_f = 3.20$ rpm and $a_p = 2.90$ deg. To limit fatigue on the active turbine components, it might be advisable to use lower amplitudes. Specifically, dynamic rotor speed forcing with $a_f = 1.12$ rpm, a value that is not large relative to the stochastic rpm variations associated with higher turbulence ABL inflow (and thus a value that should not induce unmanageable fatigue on the turbine components), could achieve 53% $(x/D)_{nl}$ reduction in a low turbulence environment of $TI = 0.02$ and 43% $(x/D)_{nl}$ reduction in a more moderate turbulence environment of $TI = 0.05$. Similar $(x/D)_{nl}$ reductions of 58 and 48%, respectively, are possible with dynamic pitch forcing of $a_p = 2.30$ deg. As discussed earlier, the $[\hat{u}'_{j1}|_m/U_\infty]/C_1$ stemming from dynamic pitch control generally have a higher margin relative to TI than those from the dynamic rotor speed control for a given $(x/D)_{nl}$, at least for the axial perturbations considered here.

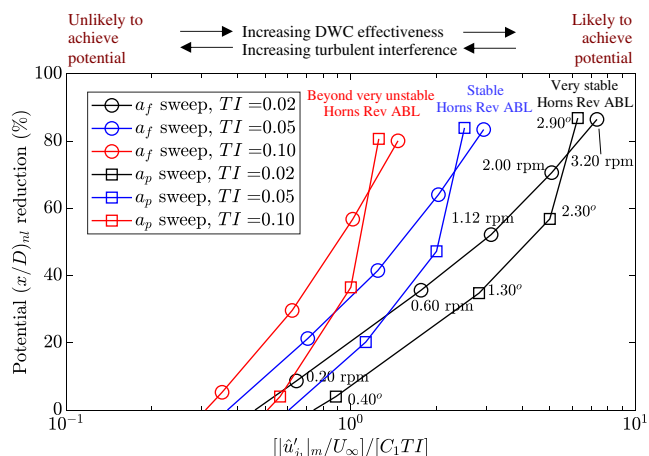


Fig. 10 Potential reduction in near-wake length $(x/D)_{nl}$ as a percent of the $(x/D)_{nl}$ from the turbulent near-wake length model of Sørensen et al. [65] vs likelihood of achieving the potential benefits with DWC in the presence of atmospheric turbulence; the likelihood is quantified as the ratio of the maximum axial perturbation magnitude, $|\hat{u}'_{j1}|_m/U_\infty$, as calculated $0.1 D$ downstream from the rotor plane in the rotating frame of reference, to the scaled turbulence intensity TI ; for visual clarity, the magnitudes of a_f and a_p are not annotated for the $TI = 0.05$ and $TI = 0.10$ cases, but these values follow the same sequences as annotated for the $TI = 0.02$ cases.

Figure 10 also shows approximate atmospheric stability categories, which derive from the offshore Horns Rev wind plant [32], for each of the TI levels plotted. These categories indicate that the effectiveness of DWC increases as the stability of the atmosphere increases, which is expected because DWC will act to compensate for missing inflow disturbances in less convective ABLs. It should be noted that the minimum ratio $[\hat{u}'_1]_m/U_\infty/[C_1 TI]$ for which DWC actions can still be effective is not known at this point, and thus, conclusions about the potential for the DWC technique in the limit of lower magnitude forcing (i.e., small numerator) or less stable ABL conditions (i.e., large denominator) can only be speculated in Fig. 10 without further work. This further work might include high-fidelity modeling and/or measurements to establish firm estimates of the $(x/D)_{nl}$ reductions that DWC can offer in various turbulent environments. It can be summarized, however, that larger-magnitude DWC actions are better both to yield potentially shorter $(x/D)_{nl}$ and higher likelihood of achieving the maximum benefits. On the other hand, fatigue damage and actuator wear also increase with the magnitude of dynamic turbine actions, and these consequences should also be the subject of future work.

VI. Conclusions

The modified midfidelity FVWM code CACTUS is used to demonstrate the effectiveness of using dynamic rotor speed and blade pitch control to accelerate the breakdown of the near wake, leading to a reduced overall wake length and ultimately allowing greater power generation for a given turbine-to-turbine spacing. Central to the approach of this study is the first-time practical application of dynamic control strategies introduced in previous work, specifically those that excite the mutual inductance instability of the tip vortices rather than bluff-body instabilities of the wake.

Stability analyses first confirmed that the harmonic forcing frequency parameter with the highest growth rate of the mutual inductance instability is $k = 1$, which corresponds to $\omega = 1.5$ for a three-bladed rotor. Using this frequency for parametric sweeps of the dynamic forcing amplitude of rotor speed, blade pitch, and tandem actions, $(x/D)_{nl}$ lengths of 0.04–1.46 were predicted over the range of rotor speed and blade pitch amplitudes considered. For the tandem cases, the phase difference between the forcing waveforms of the rotor speed and pitch was found to affect $(x/D)_{nl}$, and the most constructive superposition of waveforms occurred when $\phi_f = 90$ – 135 deg ahead of ϕ_p . Analyses that cross-referenced the DWC results with the turbulent near-wake length model of Sørensen et al. [65] indicated that $(x/D)_{nl}$ reductions of 48% with pitch forcing amplitude of $a_p = 2.30$ deg are possible within a moderately low turbulence environment of $TI = 0.05$ and that similar $(x/D)_{nl}$ reductions of 43% are possible with rotor speed forcing of $a_f = 1.12$ rpm, a value that is not large relative to the stochastic rpm variations found in more turbulent ABL inflow (and thus a value that should not induce unmanageable fatigue on the turbine components). No inherent advantage of tandem control vs individual control vectors was immediately apparent, although both individual control vectors have unique upsides: rotor speed control produces no direct mechanical wear on the blade pitch system, whereas blade pitch control may be more robust in the presence of inflow turbulence, although more investigation is required.

Additional work that might be explored with the midfidelity FVWM approach includes experimenting with different forcing waveform types (sinusoid, sawtooth, and hybrids) and duty cycles. Cases could also include combined waveforms that are superpositions of multiple individual waveforms. Higher-fidelity simulations and/or measurements are next needed to pinpoint the efficacy of DWC in the presence of inflow turbulence, as well as to understand the additional fatigue damage and structural, drivetrain, and control dynamics associated with the DWC approaches discussed earlier. Furthermore, the effect of DWC actions on the power production of the active turbine and validation of power increases in downstream turbines warrant further study.

Acknowledgments

The Wind Energy Technologies Office of the U.S. Department of Energy (DOE) is gratefully acknowledged for their funding support. This paper was prepared by Sandia National Laboratories, Albuquerque, NM. Sandia National Laboratories is a multimission laboratory managed and operated by the National Technology and Engineering Solutions of Sandia, LLC, a wholly owned subsidiary of Honeywell International, Inc., for the National Nuclear Security Administration of the U.S. DOE under contract DE-NA-0003525. This paper describes objective technical results and analysis. Any subjective views or opinions that might be expressed in the paper do not necessarily represent the views of the U.S. DOE or the U.S. Government. The first author would like to thank Steven Rodriguez for his helpful discussions surrounding the eigenvalue stability analysis and numerical stability of free-vortex wake methods, in general. The first author also expresses thanks to Phil Chiu for his guidance on best practices for modifying the CACTUS code to include dynamic wake control actions as well as to Joshua Paquette for his review of the paper.

References

- [1] Zayas, J., “Wind Overview,” *Sandia 2014 Wind Turbine Blade Workshop*, Sandia National Laboratories, Albuquerque, NM, 2014.
- [2] Nygaard, N. G., “Wakes in Very Large Wind Farms and the Effect of Neighbouring Wind Farms,” *Journal of Physics: Conference Series*, Vol. 524, No. 1, 2014, Paper 012162. <https://doi.org/10.1088/1742-6596/524/1/012162>
- [3] El-Asha, S., Zhan, L., and Iungo, G. V., “Quantification of Power Losses due to Wind Turbine Wake Interactions Through SCADA, Meteorological and Wind LiDAR Data,” *Wind Energy*, Vol. 20, No. 11, 2017, pp. 1823–1839. <https://doi.org/10.1002/we.2123>
- [4] Herges, T., Berg, J. C., Bryant, J., White, J., Paquette, J., and Naughton, B. T., “Detailed Analysis of a Waked Turbine Using a High-Resolution Scanning Lidar,” *Journal of Physics: Conference Series*, Vol. 1037, No. 7, 2018. <https://doi.org/10.1088/1742-6596/1037/7/072009>
- [5] Andersen, S. J., Lignarolo, L., Ragni, D., Ferreira, C. S., Sørensen, J. N., Mikkelsen, R. F., and Van Bussel, G., “Comparison Between PIV Measurements and Computations of the Near-Wake of an Actuator Disc,” *Journal of Physics: Conference Series*, Vol. 524, No. 1, 2014, Paper 012173. <https://doi.org/10.1088/1742-6596/524/1/012173>
- [6] Sorensen, J. N., Mikkelsen, R. F., Henningson, D. S., Ivanell, S., Sarmast, S., and Andersen, S. J., “Simulation of Wind Turbine Wakes Using the Actuator Line Technique,” *Philosophical Transactions of the Royal Society A: Mathematical, Physical and Engineering Sciences*, Vol. 373, No. 2035, 2015. <https://doi.org/10.1098/rsta.2014.0071>
- [7] Lignarolo, L., Ragni, D., Scarano, F., Ferreira, C. S., and Van Bussel, G., “Tip-Vortex Instability and Turbulent Mixing in Wind-Turbine Wakes,” *Journal of Fluid Mechanics*, Vol. 781, 2015, pp. 467–493. <https://doi.org/10.1017/jfm.2015.470>
- [8] Felli, M., Camussi, R., and Di Felice, F., “Mechanisms of Evolution of the Propeller Wake in the Transition and Far Fields,” *Journal of Fluid Mechanics*, Vol. 682, 2011, pp. 5–53. <https://doi.org/10.1017/jfm.2011.150>
- [9] Sarmast, S., Dadfar, R., Mikkelsen, R. F., Schlatter, P., Ivanell, S., Sørensen, J. N., and Henningson, D. S., “Mutual Inductance Instability of the Tip Vortices Behind a Wind Turbine,” *Journal of Fluid Mechanics*, Vol. 755, 2014, pp. 705–731. <https://doi.org/10.1017/jfm.2014.326>
- [10] Widnall, S. E., “The Stability of a Helical Vortex Filament,” *Journal of Fluid Mechanics*, Vol. 54, No. 4, 1972, pp. 641–663. <https://doi.org/10.1017/S0022112072000928>
- [11] Quaranta, H. U., Bolnot, H., and Leweke, T., “Long-Wave Instability of a Helical Vortex,” *Journal of Fluid Mechanics*, Vol. 780, 2015, pp. 687–716. <https://doi.org/10.1017/jfm.2015.479>
- [12] Sørensen, J. N., “Instability of Helical Tip Vortices in Rotor Wakes,” *Journal of Fluid Mechanics*, Vol. 682, 2011, pp. 1–4. <https://doi.org/10.1017/jfm.2011.277>
- [13] Leishman, G. J., *Principles of Helicopter Aerodynamics with CD Extra*, Cambridge Univ. Press, Cambridge, England, U.K., 2006.

- [14] Alfredsson, P. H., and Dahlberg, J., "A Preliminary Wind Tunnel Study of Windmill Wake Dispersion in Various Flow Conditions, Part 7," Aeronautical Research Inst., TN AU-1499, Sweden, 1979.
- [15] Marten, D., Paschereit, C. O., Huang, X., Meinke, M., Schroeder, W., Mueller, J., and Oberleithner, K., "Predicting Wind Turbine Wake Breakdown Using a Free Vortex Wake Code," *AIAA Journal*, Vol. 58, No. 11, 2020, pp. 1–14.
<https://doi.org/10.2514/1.J058308>
- [16] Ivanell, S., Mikkelsen, R., Sørensen, J. N., and Henningson, D., "Stability Analysis of the Tip Vortices of a Wind Turbine," *Wind Energy*, Vol. 13, No. 8, 2010, pp. 705–715.
<https://doi.org/10.1002/we.391>
- [17] Bhagwat, M. J., and Leishman, J. G., "Stability Analysis of Helicopter Rotor Wakes in Axial Flight," *Journal of the American Helicopter Society*, Vol. 45, No. 3, 2000, pp. 165–178.
<https://doi.org/10.4050/JAHS.45.165>
- [18] Rodriguez, S. N., and Jaworski, J. W., "Toward Identifying Aeroelastic Mechanisms in Near-Wake Instabilities of Floating Offshore Wind Turbines," *Journal of Energy Resources Technology*, Vol. 139, No. 5, 2017.
<https://doi.org/10.1115/1.4035753>
- [19] Tian, W., and Hu, H., "Effect of Oncoming Flow Turbulence on the Kinetic Energy Transport in the Flow Around a Model Wind Turbine," *2018 Wind Energy Symposium*, AIAA Paper 2018-0751, Jan. 2018.
<https://doi.org/10.2514/6.2018-0751>
- [20] Yang, X., Hong, J., Barone, M., and Sotiropoulos, F., "Coherent Dynamics in the Rotor Tip Shear Layer of Utility-Scale Wind Turbines," *Journal of Fluid Mechanics*, Vol. 804, 2016, pp. 90–115.
<https://doi.org/10.1017/jfm.2016.503>
- [21] Hermesen, B. L., Bornemeier, M., and Luznik, L., "Near Wake Development Behind Marine Propeller Model in Presence of Freestream Turbulence," *Journal of Fluids Engineering*, Vol. 142, No. 5, 2020.
<https://doi.org/10.1115/1.4045854>
- [22] Hancock, P., Zhang, S., Pascheke, F., and Hayden, P., "Wind Tunnel Simulation of a Wind Turbine Wake in Neutral, Stable and Unstable Wind Flow," *Journal of Physics: Conference Series*, Vol. 555, No. 1, 2014, Paper 012047.
https://doi.org/10.1007/978-3-642-54696-9_16
- [23] Chamorro, L. P., and Porté-Agel, F., "Effects of Thermal Stability and Incoming Boundary-Layer Flow Characteristics on Wind-Turbine Wakes: A Wind-Tunnel Study," *Boundary-Layer Meteorology*, Vol. 136, No. 3, 2010, pp. 515–533.
<https://doi.org/10.1007/s10546-010-9512-1>
- [24] Magnusson, M., and Smedman, A.-S., "Air Flow Behind Wind Turbines," *Journal of Wind Engineering and Industrial Aerodynamics*, Vol. 80, Nos. 1–2, 1999, pp. 169–189.
[https://doi.org/10.1016/S0167-6105\(98\)00126-3](https://doi.org/10.1016/S0167-6105(98)00126-3)
- [25] Zhang, W., Markfort, C. D., and Porté-Agel, F., "Wind-Turbine Wakes in a Convective Boundary Layer: A Wind-Tunnel Study," *Boundary-Layer Meteorology*, Vol. 146, No. 2, 2013, pp. 161–179.
<https://doi.org/10.1007/s10546-012-9751-4>
- [26] Churchfield, M. J., Lee, S., Michalakes, J., and Moriarty, P. J., "A Numerical Study of the Effects of Atmospheric and Wake Turbulence on Wind Turbine Dynamics," *Journal of Turbulence*, No. 13, 2012, p. N14.
<https://doi.org/10.1080/14685248.2012.668191>
- [27] Abkar, M., and Porté-Agel, F., "Influence of Atmospheric Stability on Wind-Turbine Wakes: A Large-Eddy Simulation Study," *Physics of Fluids*, Vol. 27, No. 3, 2015, Paper 035104.
<https://doi.org/10.1063/1.4913695>
- [28] Bhaganagar, K., and Debnath, M., "The Effects of Mean Atmospheric Forcings of the Stable Atmospheric Boundary Layer on Wind Turbine Wake," *Journal of Renewable and Sustainable Energy*, Vol. 7, No. 1, 2015.
<https://doi.org/10.1063/1.4907687>
- [29] Jha, P. K., Duque, E. P., Bashioiu, J. L., and Schmitz, S., "Unraveling the Mysteries of Turbulence Transport in a Wind Farm," *Energies*, Vol. 8, No. 7, 2015, pp. 6468–6496.
<https://doi.org/10.3390/en8076468>
- [30] Kelley, C. L., and Ennis, B. L., "SWiFT Site Atmospheric Characterization," Sandia National Lab. (SNL-NM) TR SAND-2016-0216, Albuquerque, NM, 2016.
<https://doi.org/10.2172/1237403>
- [31] Barthelmie, R. J., and Jensen, L., "Evaluation of Wind Farm Efficiency and Wind Turbine Wakes at the Nysted Offshore Wind Farm," *Wind Energy*, Vol. 13, No. 6, 2010, pp. 573–586.
<https://doi.org/10.1002/we.408>
- [32] Hansen, K. S., Barthelmie, R. J., Jensen, L. E., and Sommer, A., "The Impact of Turbulence Intensity and Atmospheric Stability on Power Deficits due to Wind Turbine Wakes at Horns Rev Wind Farm," *Wind Energy*, Vol. 15, No. 1, 2012, pp. 183–196.
<https://doi.org/10.1002/we.512>
- [33] Kelley, C. L., Maniaci, D. C., and Resor, B. R., "Horizontal-Axis Wind Turbine Wake Sensitivity to Different Blade Load Distributions," *33rd Wind Energy Symposium*, AIAA Paper 2015-0490, Jan. 2015.
<https://doi.org/10.2514/6.2015-0490>
- [34] Castillo-Castellanos, A., Venegas, E. D., and Le Dizès, S., "Joukowski's Wake Model for Tip-Splitting Rotors," *Journal of Physics: Conference Series*, Vol. 1934, No. 1, 2021, Paper 012005.
<https://doi.org/10.1088/1742-6596/1934/1/012005>
- [35] Schröder, D., Leweke, T., Hörschemeyer, R., and Stumpf, E., "Instability and Merging of a Helical Vortex Pair in the Wake of a Rotor," *Journal of Physics: Conference Series*, Vol. 1934, No. 1, 2021, Paper 012007.
<https://doi.org/10.1088/1742-6596/1934/1/012007>
- [36] Bastankhah, M., and Abkar, M., "Multirotor Wind Turbine Wakes," *Physics of Fluids*, Vol. 31, No. 8, 2019, Paper 085106.
<https://doi.org/10.1063/1.5097285>
- [37] van der Laan, M. P., Andersen, S. J., Ramos García, N., Angelou, N., Pirrung, G. R., Ott, S., Sjöholm, M., Sørensen, K. H., Vianna Neto, J. X., and Kelly, M., "Power Curve and Wake Analyses of the Vestas Multi-Rotor Demonstrator," *Wind Energy Science*, Vol. 4, No. 2, 2019, pp. 251–271.
<https://doi.org/10.5194/wes-4-251-2019>
- [38] Munters, W., and Meyers, J., "Towards Practical Dynamic Induction Control of Wind Farms: Analysis of Optimally Controlled Wind-Farm Boundary Layers and Sinusoidal Induction Control of First-Row Turbines," *Wind Energy Science*, Vol. 3, No. 1, 2018, pp. 409–425.
<https://doi.org/10.5194/wes-3-409-2018>
- [39] Yilmaz, A. E., and Meyers, J., "Optimal Dynamic Induction Control of a Pair of Inline Wind Turbines," *Physics of Fluids*, Vol. 30, No. 8, 2018, Paper 085106.
<https://doi.org/10.1063/1.5038600>
- [40] Houck, D., and Cowen, E., "Can You Accelerate Wind Turbine Wake Decay with Unsteady Operation?," *AIAA SciTech 2019 Forum*, AIAA Paper 2019-2084, Jan. 2019.
<https://doi.org/10.2514/6.2019-2084>
- [41] Wang, C., Campagnolo, F., Sharma, A., and Bottasso, C., "Effects of Dynamic Induction Control on Power and Loads, by LES-ALM Simulations and Wind Tunnel Experiments," *Journal of Physics: Conference Series*, Vol. 1618, No. 2, 2020, Paper 022036.
<https://doi.org/10.1088/1742-6596/1618/2/022036>
- [42] Frederik, J. A., Weber, R., Cacciola, S., Campagnolo, F., Croce, A., Bottasso, C., and Wingerden, J.-W. V., "Periodic Dynamic Induction Control of Wind Farms: Proving the Potential in Simulations and Wind Tunnel Experiments," *Wind Energy Science*, Vol. 5, No. 1, 2020, pp. 245–257.
<https://doi.org/10.5194/wes-5-245-2020>
- [43] Cacciola, S., Bertozzi, A., Sartori, L., and Croce, A., "On the Dynamic Response of a Pitch/Torque Controlled Wind Turbine in a Pulsating Dynamic Wake," *Journal of Physics: Conference Series*, Vol. 1618, No. 6, 2020, Paper 062033.
<https://doi.org/10.1088/1742-6596/1618/6/062033>
- [44] Odemark, Y., and Fransson, J. H., "The Stability and Development of Tip and Root Vortices Behind a Model Wind Turbine," *Experiments in Fluids*, Vol. 54, No. 9, 2013, p. 1591.
<https://doi.org/10.1007/s00348-013-1591-6>
- [45] Jonkman, J., Butterfield, S., Musial, W., and Scott, G., "Definition of a 5-MW Reference Wind Turbine for Offshore System Development," National Renewable Energy Lab., TR NREL/TP-500-38060, Golden, CO, 2009.
<https://doi.org/10.2172/947422>
- [46] Jonkman, J., "DOWEC-NREL 5MW Blade Airfoil Data-v2," NREL National Wind Technology Center, 2012, <https://wind.nrel.gov/forum/wind/download/file.php?id=305&sid=5c5e9a9806fbb5667d0d3cf4383b2c4a> [retrieved 19 Sept. 2020].
- [47] Schmitz, S., *Aerodynamics of Wind Turbines: A Physical Basis for Analysis and Design*, Wiley, New York, 2020.
- [48] Bhagwat, M. J., and Leishman, J. G., "Stability, Consistency and Convergence of Time-Marching Free-Vortex Rotor Wake Algorithms," *Journal of the American Helicopter Society*, Vol. 46, No. 1, 2001, pp. 59–71.
<https://doi.org/10.4050/JAHS.46.59>
- [49] Ramos-García, N., Spietz, H. J., Sørensen, J. N., and Walther, J. H., "Vortex Simulations of Wind Turbines Operating in Atmospheric Conditions Using a Prescribed Velocity-Vorticity Boundary Layer Model," *Wind Energy*, Vol. 21, No. 11, 2018, pp. 1216–1231.
<https://doi.org/10.1002/we.2225>

- [50] Kleusberg, E., Benard, S., and Henningson, D. S., "Tip-Vortex Breakdown of Wind Turbines Subject to Shear," *Wind Energy*, Vol. 22, No. 12, 2019, pp. 1789–1799.
<https://doi.org/10.1002/we.2403>
- [51] Rodriguez, S. N., Jaworski, J. W., and Michopoulos, J. G., "Stability of Helical Vortex Structures Shed from Flexible Rotors," *Journal of Fluids and Structures*, Vol. 104, 2021, Paper 103279.
<https://doi.org/10.1016/j.jfluidstructs.2021.103279>
- [52] Murray, J., and Barone, M., "The Development of Cactus, a Wind and Marine Turbine Performance Simulation Code," *49th AIAA Aerospace Sciences Meeting Including the New Horizons Forum and Aerospace Exposition*, AIAA Paper 2011-0147, June 2011.
<https://doi.org/10.2514/6.2011-147>
- [53] Murray, J. C., and Barone, M., *CACTUS User's Manual*, Sandia National Lab., Albuquerque, NM, 2013.
- [54] Strickland, J. H., Webster, B., and Nguyen, T., "A Vortex Model of the Darrieus Turbine: An Analytical and Experimental Study," *Journal of Fluids Engineering*, Vol. 101, No. 4, Dec. 1979, pp. 500–505.
<https://doi.org/10.1115/1.3449018>
- [55] Katz, J., and Plotkin, A., *Low-Speed Aerodynamics*, Cambridge Univ. Press, Cambridge, England, U.K., 2001.
- [56] Gormont, R. E., *A Mathematical Model of Unsteady Aerodynamics and Radial Flow for Application to Helicopter Rotors*, Boeing Vertol, Philadelphia, PA, 1973.
- [57] Rodriguez, S. N., "Stability and Dynamic Properties of Tip Vortices Shed from Flexible Rotors of Floating Offshore Wind Turbines," Ph.D. Dissertation, Lehigh Univ., Bethlehem, PA, 2018.
- [58] Burton, T., Jenkins, N., Sharpe, D., and Bossanyi, E., *Wind Energy Handbook*, Wiley, New York, 2011.
- [59] Maniaci, D. C., "Wind Turbine Design Using a Free-Wake Vortex Method with Winglet Application," Aerospace Engineering, Ph.D. Dissertation, Pennsylvania State Univ., State College, PA, 2012.
- [60] Jonkman, J., and Musial, W., "Offshore Code Comparison Collaboration (OC3) for IEA Wind Task 23 Offshore Wind Technology and Deployment," National Renewable Energy Lab. TR NREL/TP-5000-48191, Golden, CO, 2010.
<https://doi.org/10.2172/1004009>
- [61] Leroy, V., Gilloteaux, J.-C., Philippe, M., Babarit, A., and Ferrant, P., "Development of a Simulation Tool Coupling Hydrodynamics and Unsteady Aerodynamics to Study Floating Wind Turbines," *Proceedings of the ASME 2017 36th International Conference on Ocean, Offshore and Arctic Engineering*, Vol. 10, 2017, p. V010T09A040.
<https://doi.org/10.1115/OMAEE2017-61203>
- [62] Leroy, V., Gilloteaux, J. C., Lynch, M., Babarit, A., and Ferrant, P., "Impact of Aerodynamic Modeling on Seakeeping Performance of a Floating Horizontal Axis Wind Turbine," *Wind Energy*, Vol. 22, No. 8, 2019, pp. 1019–1033.
<https://doi.org/10.1002/we.2337>
- [63] Neary, V. S., Gunawan, B., Michelen, C., Fontaine, A. A., Bachant, P., Wosnik, M., Straka, B., and Meyer, R., "US Department of Energy (DOE) National Lab Activities in Marine Hydrokinetics: Scaled Model Testing of DOE Reference Turbines," Sandia National Lab., SAND2013-7242C, Albuquerque, NM, 2013, <https://www.osti.gov/biblio/1108177>.
- [64] Jonkman, B., Historical NWTC Repositories, Vol. 2021, Nov. 11, 2016, https://github.com/old-NWTC/FAST/tree/master/CertTest/5MW_Baseline [retrieved 1 Aug. 2021].
- [65] Sørensen, J. N., Mikkelsen, R., Sarmast, S., Ivanell, S., and Henningson, D., "Determination of Wind Turbine Near-Wake Length Based on Stability Analysis," *Journal of Physics: Conference Series*, Vol. 524, No. 1, 2014, Paper 012155.
<https://doi.org/10.1088/1742-6596/524/1/012155>

F. N. Coton
Associate Editor